

Thesis for the Degree of Doctor of Philosophy

**MHD Simulation Studies of Solar Flux Ropes with
Dynamic State Transition and Their Propagation in
the Interplanetary Space**

Junmo An

School of Space Research
Graduate School
Kyung Hee University
Seoul, Korea

February, 2020

Abstract

A solar active region (AR) is the region where various kinds of active phenomena tend to occur, such as solar flares and coronal mass ejections (CMEs). It has been known that an AR is formed via flux emergence from the convection zone. Although it has been observationally shown that an AR slowly evolve for weeks or even months before flares and CMEs suddenly occur, the triggering mechanism of such eruptive events is still not clear. A CME entered the interplanetary space, called interplanetary CME (ICME), sometimes travels toward the Earth, causing space weather disturbances as it interacts with the Earth's magnetosphere. These disturbances potentially damage spaceborne and ground-based systems and services. Regarding these topics, we focus on two questions: 1) how does the solar flux rope that eventually develops to an ICME evolve from the quasi-static state to the dynamic state (dynamic state transition); 2) how do ICME properties in the interplanetary space affect the space weather disturbances in the vicinity of the Earth.

Firstly, we performed a three-dimensional magnetohydrodynamic (MHD) simulation to investigate the dynamic state transition of a solar flux rope. In this simulation, we obtained a flux rope by reproducing flux emergence from the solar convection zone into the solar corona. In order to investigate the dynamic evolution of emerging magnetic field in the corona, we used two key parameters κ and H , the former of which represents the curvature of an emerging magnetic field line and while the latter the scale height of emerging magnetic field strength along the symmetry axis of an emerged magnetic loop. Here κ is related to downward magnetic tension force, while $1/H$ is related to upward magnetic pressure force. The plot of κ and H along the symmetry axis shows that they tend to increase with height until they reach their common peak. Below the location of the common peak, $1/H$ tend to be almost balanced by κ , whereas above that location, $1/H$ tends to exceeds κ , suggesting that upward magnetic pressure force is dominant over the downward magnetic tension force. When the flux rope axis exceeds the peak, it experiences the dynamic transition from a quasi-static state in which the upward and downward forces are balanced to an eruptive state. We also investigated the torus instability and compared to the

dynamic state transition that we proposed.

Secondly, we performed an MHD simulation to investigate the relation between ICME properties and space weather disturbances in the vicinity of the Earth. Toward this end, we used a spheromak-shaped ICME model parametrized by the injection speed, mass, location, magnetic field strength, and magnetic field orientation. The parameter values were determined based on a halo CME event observed on 10 September 2014 by Large Angle and Spectrometric Coronagraph (LASCO) on board the Solar and Heliospheric Observatory (SOHO). We simulated the ICME travelling through a background solar wind reconstructed via an MHD-interplanetary scintillation (MHD-IPS) tomography method with the photospheric magnetogram data and IPS data. We compared simulation results to in situ observations in the vicinity of the Earth and discussed how the arrival time and solar wind profiles associated with the ICME vary with the properties of the ICME.

Keywords:

magnetohydrodynamics (MHD) — Sun: corona — Sun: magnetic fields — Sun: solar wind — Sun: coronal mass ejections (CMEs) — Sun: solar–terrestrial relations

Table of Contents

ABSTRACT	I
TABLE OF CONTENTS	III
LIST OF FIGURES.....	V
LIST OF TABLES.....	V
CHAPTER 1 INTRODUCTION	1
1.1 EMERGENCE OF SOLAR MAGNETIC FIELDS	1
1.2 CORONAL MASS EJECTION	3
1.3 INTERPLANETARY CMEs (ICMEs) AND MAGNETIC CLOUD.....	8
1.4 MOTIVATION AND OBJECTIVE.....	10
1.5 ORGANIZATION	11
CHAPTER 2 STABILITY AND DYNAMICS OF A FLUX ROPE FORMED VIA FLUX EMERGENCE INTO THE SOLAR ATMOSPHERE.....	12
2.1 INTRODUCTION	12
2.2 MODEL.....	15
2.3 RESULTS	20
2.3.1 <i>Overview of the Simulation</i>	20
2.3.2 <i>Curvature and Scale Height Analysis of Emerging Magnetic Field</i>	20
2.3.3 <i>Decay Index Analysis for the Torus Instability</i>	27
2.4 DISCUSSION	29
CHAPTER 3 PARAMETRIC STUDY OF ICME PROPERTIES RELATED TO SPACE WEATHER DISTURBANCES VIA A SERIES OF THREE-DIMENSIONAL MHD SIMULATIONS.....	36
3.1 INTRODUCTION	36
3.2 OBSERVATIONS AND MODEL	38
3.2.1 <i>Observations</i>	38
3.2.2 <i>Model</i>	39
3.3 RESULTS	48

3.3.1 <i>Standard Reference Case</i>	48
3.3.2 <i>Comparison to the Standard Reference Case</i>	52
3.3.3 <i>Sensitivity of ICME Arrival Time to Each Parameter</i>	53
3.4 SUMMARY AND DISCUSSION	58
CHAPTER 4 SUMMARY	61
BIBLIOGRAPHY	63
ABSTRACT (KOREAN)	73
ACKNOWLEDGEMENT (KOREAN)	76

List of Figures

Figure 1.1 Structure of the Sun (adapted from https://en.wikipedia.org/wiki/Sun).	2
Figure 1.2 An illustration of the emergence of a flux rope from the solar convection zone.	2
Figure 1.3 An image of a CME that occurred on 27 Feb. 2000. The central white circle indicates the photosphere of the Sun (adapted from https://apod.nasa.gov/apod/).....	5
Figure 1.4 Several solar eruption models. (a) Loss-of-equilibrium model (from Forbes and Isenberg, 1991). (b) Tether cutting model (from Moore et al., 2011). (c) Kink instability (from Torok and Kliem, 2005).	6
Figure 1.5 An illustration of the breakout model. (a) Initial quadrupolar potential field state with no free energy. (b) Central arcade field lines expand due to photospheric shearing motion, and the breakout current sheet is produced. (c) As central arcade fields rise, the flare current sheet is produced, the eruption occurs (from Karpen et al., 2012).....	7
Figure 1.6 In situ measurements of a magnetic cloud. Index for the associated geomagnetic storm (Dst), the magnetic field strength ($ B $), the latitude (Θ_B), longitude (Φ_B) of the cloud, proton density (N_p), proton thermal speed, flow speed, and the plasma beta are shown from top to bottom. The passage time of the shock and magnetic cloud at the Earth is marked by ‘S’ and ‘MC’ at the top (from Gopalswamy, 2006).	9
Figure 2.1 Initial distributions of gas density (dashed line), pressure (dotted line), temperature (dot-dashed line), and magnetic pressure (solid line) along z -axis.....	19
Figure 2.2 Snapshots of an emerging flux tube taken at $t = 16$, $t = 22$, $t = 41$, and $t = 50$. Magnetic field lines are given in green, while the red line represents the axis of the flux tube. Gray-scale maps at $z = 0$ indicate photospheric magnetic flux.	23
Figure 2.3 (a) Distributions along z -axis of κ (solid line) and $1/H$ (dashed line) in the top panel, B_x in the middle panel, and $\log_{10}P_m$ in the bottom panel at $t=41$ are shown. The vertical line in the top panel indicates the location of the axis of the rising flux rope. (b) Same as (a) but for $t = 44$	24
Figure 2.4 (c) Same as Figure 2.3(a) but for $t = 47$. (d) Same as Figure 2.3(a) but for $t = 50$	25
Figure 2.5 Temporal developments of the location (solid line) and velocity (dashed line) of the axis of the rising flux rope, measured at z -axis.	26

Figure 2.6 (a) Distributions of the decay index along z -axis are presented for extrapolated potential field at $t = 41$ (solid line), 44 (dotted line), 47 (dashed line), and 50 (dot-dashed line). The diamonds indicate the locations of the axis of the rising flux rope at these times. 28

Figure 2.7 (a) Distributions of κ and $1/H$ along z -axis are presented for a bipolar potential field. The normalization unit of length is given by a distance between positive and negative poles placed at $z = 0$. P, Q, and R represent the field lines indicated in Figure 2.7(b). (b) Configuration of the potential field is presented. 32

Figure 2.8 (a) Spatial distributions of κ (solid line) and $1/H$ (dotted line) are schematically illustrated for emerging field. S and S' represent the field lines outlined by thick red lines. The dotted blue lines indicate the field lines at the maximum of κ . (b) Evolution of emerging field lines in a limited lateral expansion shape (left) and fan expansion shape (right). Adapted from Magara (2004). 33

Figure 2.9 Temporal development of aspect ratio for the axis of the rising flux rope 34

Figure 2.10 Distributions of κ along z -axis are presented for the potential field explained in Section 2.3.3. Times are $t = 41$ (top), 44 (second from the top), 47 (third from the top), and 50 (bottom). The solid and dotted vertical lines in each panel represent the location of the axis of the rising flux rope and the location of maximum κ for the emerging field reproduced by the simulation. The diamond and dashed vertical line in each panel show the locations of maximum κ and $n = 1.5$ for that potential field. 35

Figure 3.1 Synoptic maps of the: (a) radial flow speed, (b) temperature, (c) number density, (d) radial magnetic field component at the inner boundary ($50 R_s$ apart from the center of the Sun). The plus sign indicates the expected location of the ICME. 42

Figure 3.2 Distributions of: (a) temperature, (b) number density, (c) radial flow speed, (d) magnetic field strength. These parameters are shown in the reconstructed solar wind on the solar equatorial plane bounded by the *inner circle* ($50 R_s$ apart from the center of the Sun) and the *outer circle* ($250 R_s$ apart from the center of the Sun). The *plus sign* and *circle* indicate the expected location of the ICME at $50 R_s$ and the location of the Earth, respectively. 43

Figure 3.3 Snapshots of the ICME traveling through the interplanetary space taken at two different times. The *color maps* show the distribution of radial flow speed on the solar

equatorial plane, while field lines are drawn *in gray-scale colors* representing the B_z component. The units of the radial flow speed, the B_z component, and time are 91 km s^{-1} , 1000 nT , and 5.7 hr , respectively. 50

Figure 3.4 Simulated (*green*) and observed (OMNI 2, *dotted*) 2.5-day temporal profiles of magnetic field strength, three components of the magnetic field, flow speed, temperature, and number density obtained at the Earth. The *vertical solid line* indicates the arrival time of the ICME shock, while the range bounded by the *two vertical dashed lines* represents the period during which the MC passed through the Earth. 51

Figure 3.5 (a) Same as Figure 3.4 except that the injection speed of the ICME is higher (*red*), the same (*green*), and lower (*blue*). (b) Same as Figure 3.4 except that the mass of the ICME is larger (*red*), the same (*green*), and smaller (*blue*). 55

Figure 3.6 (a) Same as Figure 3.4 except that the longitude of the source region is western (*red*), the same (*green*), and eastern (*blue*) from the standard reference case. (b) Same as Figure 3.4 except that the latitude of the source region is northern (*red*), the same (*green*), and southern (*blue*) from the standard reference case. 56

Figure 3.7 (a) Same as Figure 3.4 except that the magnetic field strength of the ICME is stronger (*red*), the same (*green*), weaker (*blue*) than in the standard reference case. (b) Same as Figure 3.4 except that the magnetic field orientation of the ICME is south-north (*red*), the same (*green*), north-south (*blue*) when compared to the standard reference case. 57

List of Tables

Table 2.1 Units of Physical Quantities	18
Table 3.1 Parameter set of the standard reference case	47
Table 3.2 Sets of parameters for the parametric study and results	49

Chapter 1 Introduction

1.1 Emergence of Solar Magnetic Fields

Solar magnetic fields are a key ingredient of various kinds of active phenomena on the Sun, such as solar flares, jets, and coronal mass ejections (CMEs). It is therefore important to understand how these magnetic fields are formed in the solar interior (Figure 1.1), emerge to the solar surface and produce solar active regions (ARs). Results from the helioseismology show that the magnetic fields are probably amplified at the base of the convection zone, called tachocline (Spiegel and Zahn, 1992), due to strong shear flows there. The magnetic fields in the convection zone then emerge to the solar surface by the magnetic buoyancy (Parker, 1955) and produce ARs.

The buoyancy of the magnetic fields could be understood as follows. Suppose that a magnetic flux tube has formed in the convection zone with gas pressure p_i and magnetic field strength B_i (Figure 1.2). The total pressure (gas pressure + magnetic pressure) balance in the lateral direction of the tube requires

$$p_i + \frac{B_i^2}{8\pi} = p_e, \quad (1.1)$$

where, p_e is the external gas pressure outside the tube. If the temperature of the structures are uniform ($T_i = T_e = T$), and using the perfect gas law, the internal density ρ_i should be smaller than the external density ρ_e . This produces a buoyancy force of $(\rho_e - \rho_i)g$ and make the tube rises, where g is the solar gravity. Once the tube starts to rise and its shape is curved, the tube also feels downward magnetic tension force ($B_i^2/4\pi L$, where L is the length of the tube), making short flux tubes difficult to rise.

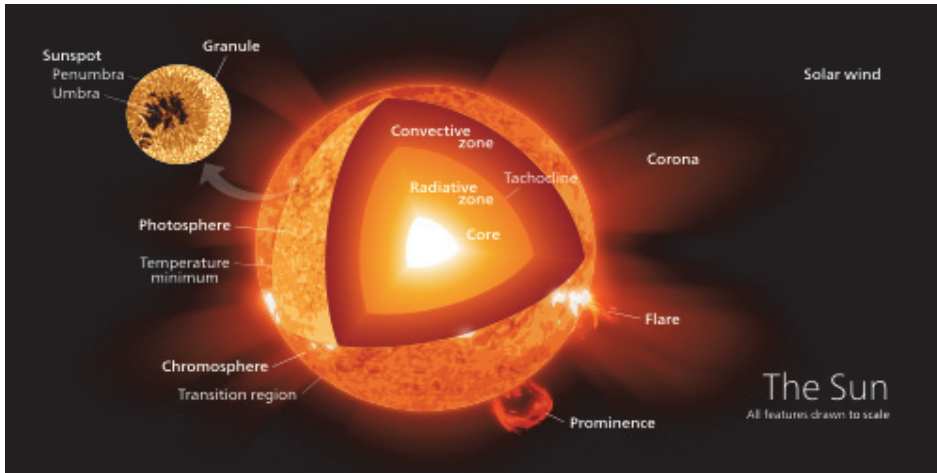


Figure 1.1 Structure of the Sun (adapted from <https://en.wikipedia.org/wiki/Sun>).

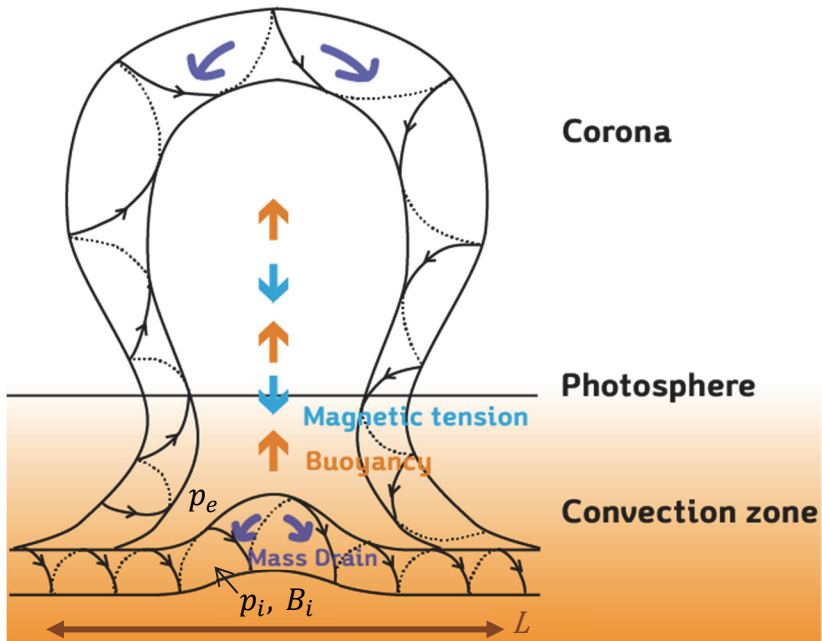


Figure 1.2 An illustration of the emergence of a flux rope from the solar convection zone.